Visible-Light Induced Sustainable Water Treatment Using Plasmo-Semiconductor Nanogap Bridge Array, PNA

Emma Murphy, Yunbo Liu, Daniel Krueger, Meghna Prasad, Somin Eunice Lee,* and Younggeun Park*

The development of sustainable methods for energy-intensive water treatment processes continues to be a challenging issue. Plasmonic-semiconductor nanoparticles, which absorb large amounts of sunlight in the visible range for conversion into chemical energy efficiently, can form the basis of a sustainable water treatment method. However, the potential uses of plasmonic semiconductor particles for water treatment have not been fully explored yet because of the limitations associated with the imbalance between light capture, charge transfer, and the required recycling steps for the particles themselves. Herein, a significantly improved visible-light-induced water treatment method that uses a plasmo-semiconductor nanogap bridge array (PNA) is reported. As an arrangement of antenna-reactors, the PNA enables the balancing of the largely enhanced electromagnetic field in the plasmonic nanogap coupling region and optimal separation of charge carriers in the semiconductor. The simultaneous effects of visible-light absorption and charge transfer lead to the generation of a highly enhanced visible-light-induced OH radical ($\bullet$OH). Consequently, visible-light-induced 5-log N/N_0 water disinfection and 100% chemical decomposition for sustainable water treatment were demonstrated. Owing to the large light absorption, charge carrier utilization, and array-oriented scalability, the PNA will be valuable in various sustainable energy and environmental applications.

1. Introduction

The utilization of solar energy driven by plasmonic nanostructures is attracting a great deal of attention for applications involving sustainable energy and environmental processes. In particular, the strong absorption/scattering stemming from localized surface plasmon resonance (LSPR) in plasmonic nanostructures can enable various sustainable solar-energy based technologies.

Recent studies have demonstrated the promising capabilities of such plasmonic nanostructures in LSPR-induced hot electrons, in which the nanostructures are useful for energy conversion and storage when combined with electron-accepting semiconductors such as plasmonic metallic-semiconductor nanostructures.[16] Hot electrons generated in semiconductor-plasmonic nanostructure (NS) composites have been shown to play a central role in increasing the efficiency of solar energy conversion because these materials allow for the tuning of the wavelength over a wide region in the visible to near-infrared (NIR) region by controlling the physical shape of the NSs.[7,8] The underlying principle is mainly related to the surface plasmon energy transfer, in which the SP state of the metallic structure induces charge separation in the neighboring semiconductor, and this enables the solar energy conversion process. Plasmon-derived hot charge carriers in metallic nanostructures are transmitted to the semiconductor under visible light illumination.[9–13] As a result of the hole/electron charge carrier separation regardless of its bandgap energy, interfacial chemical transformation occurs. In accordance with this principle, the plasmonic metallic-semiconductor nanostructure holds

E. Murphy, M. Prasad
Department of Civil and Environmental Engineering
University of Michigan
Ann Arbor, MI 48109, USA

Y. Liu, Prof. S. E. Lee
Department of Electrical & Computer Engineering
Department of Biomedical Engineering
Biointerfaces Institute, Macromolecular Science and Engineering
University of Michigan
Ann Arbor, MI 48109, USA
E-mail: sleee@umich.edu

The ORCID identification number(s) for the author(s) of this article can be found under https://doi.org/10.1002/smll.202006044.

D. Krueger
Department of Chemical Engineering
University of Michigan
Ann Arbor, MI 48109, USA

Prof. S. E. Lee
Biointerfaces Institute
University of Michigan
Ann Arbor, MI 48109, USA

Dr. Y. Park
Department of Mechanical Engineering
University of Michigan
Ann Arbor, MI 48109, USA
E-mail: ygpark@umich.edu

**ADVANCED
SCIENCE NEWS**
www.advancedsciencenews.com

NANO · MICRO
small
www.small-journal.com

great potential for future solar water remediation processes by allowing for the production of reactive oxygen species (ROS), for example, hydroxyl radicals (OH), which can react unselectively and instantaneously with the surrounding toxic ingredients, such as undesirable organic compounds and biological species, and aid in their elimination.[14] Traditionally, the production of ROS requires high levels of energy consumption to achieve sufficient performance in conventional water treatment processes; however, the visible-light-induced production of ROS would allow for the transition to solar water treatment as a sustainable process.[15]

To date, there have been many efforts to explore energy transfer between plasmonics and semiconductor materials.[16–19] Most plasmonic-semiconductor studies in energy and environmental applications have been based on particles which have been synthesized using chemical synthesis techniques and overgrowth approaches. Although these particles showed a great control of the geometry, to achieve both of the large enhancement of electromagnetic field in the plasmonic structure and optimal separation of charge carriers in the semiconductor, precise design of interparticle distance and nanogap in the plasmonic-semiconductor structure have to be addressed. In addition, unlike gas-phase reaction which has been mostly explored, water treatment using the plasmonic semiconductor nanoparticles necessitates postprocessing to can recycle nanoparticles within the mixture solution after the photoreaction.

Despite the growing interest in this topic, the possibility of using plasmonic metallic semiconductor nanostructures in water treatment applications has not been explored. To make such a sustainable water treatment process feasible, a comprehensive approach to engineering geometry of plasmonic semiconductor structure that combines the solar energy capture, hot-electron generation, and energy transfer phases in an array type within large-area substrates will be required.

In this study, we report significantly enhanced visible-light-induced water treatment effects resulting from the use of an array of plasmo-semiconductor nanogap bridge array (PNA) (**Figure 1**). We systematically characterized the optical properties of the PNA, which showed strong plasmonic coupling in the nanogap and thereby increased visible-light absorption. In addition, we demonstrated enhanced plasmon resonance energy transfer (PRET) in the multi-dimensional metal-semiconductor structure resulting from the plasmonic nanogap of the TiO$_2$ layer. Finally, we showed that greatly enhanced generation of OH radicals results in significant improvements in bacterial inactivation by the multidimensional metal-semiconductor nanostructure array.

2. Results and Discussions

For optimal photocatalytic reaction, the metallic-semiconductor nano structures should be designed not only to maximize local field enhancement at the catalytic interface but also to optimize transfer of charge carriers where charge separation and surface reaction occurs. The metallic-semiconductor nanostructure array for this study was designed to exploit this type of coupling.

2.1. Multidimensional Plasmonic Semiconductor Array Fabrication and Characterization

In the PNA geometry, the coupled AuNS array induces a highly focused local electromagnetic (*E*)-field. The hot electrons in the plasmonic nanostructure to the nanogap of TiO$_2$ generate highly energetic charge carriers' separation. The separated charges then diffuse into the interface between the PNA and H$_2$O.[7,8,10,20,21] In this geometry, the plasmonic nanogap of TiO$_2$ determines plasmonic coupling between top/bottom AuNS and the charge separation.

We constructed the PNA in the multidimensional arrays of AuNS by combining thermal dewetting and evaporating of the nanostructure (**Figure 2**). This approach enabled control of the plasmonic nanogap ($\delta_{nanogap}$) between the first and second AuNS array layers due to TiO$_2$ layers with thickness variation from 1 to 30 nm (Figure 2a; Figure S1, Supporting Information). To ensure the crystallinity of the TiO$_2$ layer, a thermal treatment step then followed.[22] Subsequently, we characterized the fabricated structure. First, the fabricated PNA ($\delta_{nanogap}$ = 8) has a hemispherical bump structure array within ≈20 nm height profile as determined by atomic force microscopy (AFM) (Figure 2b). The scanning electron microscopy (SEM) images show that the AuNS array consisted of thin asymmetric spheres with an average interparticle distance of ≈45 nm (<≈20% standard deviation) and uniform distribution in the size (d_{PNA} = 40 nm ± 25%) with high density (ρ_{PNA} ≈ 880 AuNSs/µm^2) (Figure 2c). After adding the TiO$_2$ layer as a plasmonic nanogap on the first AuNS array, the second (top) AuNS array were prepared, sequentially. The SEM images of TiO$_2$/AuNS and PNA ($\delta_{nanogap}$ = 8 nm) from the top-view reveals similar distribution of that from the first AuNS array. The energy-dispersive X-ray spectroscopy (EDS) elemental analysis of the PNA samples reveals identifiable components of the layered nanostructures. The acquired EDS spectrum from the PNA on a glass substrate clearly shows Au, Ti, and O elements including glass elements (Si, Na, and Mg) (Figure 2d). The counts of Ti increase with $\delta_{nanogap}$ from 1 to 30 nm. The cross-sectional SEM images of different $\delta_{nanogap}$ shows that the thickness of the TiO$_2$ nanogap layer increased with $\delta_{nanogap}$ (Figure 2e; Figure S2, Supporting Information). We plotted the measured $\delta_{nanogap}$ in the PNA samples as a function of the deposition condition used in the fabrication process. The data show that on average deposition rate results in 0.1 nm min^{-1} of TiO$_2$. The measured $\delta_{nanogap}$ shows a linear trend with the process condition while the AuNSs shows uniform sizes. The top and bottom AuNS arrays showed consistent hemispherical shape, size (40 nm ± 13%), and interparticle distance (45 nm ± 11%). The diameter of AuNS on the top layer shows minimal change as a function of the $\delta_{nanogap}$ between 1 and 30 nm. The AuNS particle size distribution analysis also showed a minimal change with the $\delta_{nanogap}$ variation (Figure 2f). These results support the successful fabrication of a PNA structure exhibiting high density and uniform size distribution.

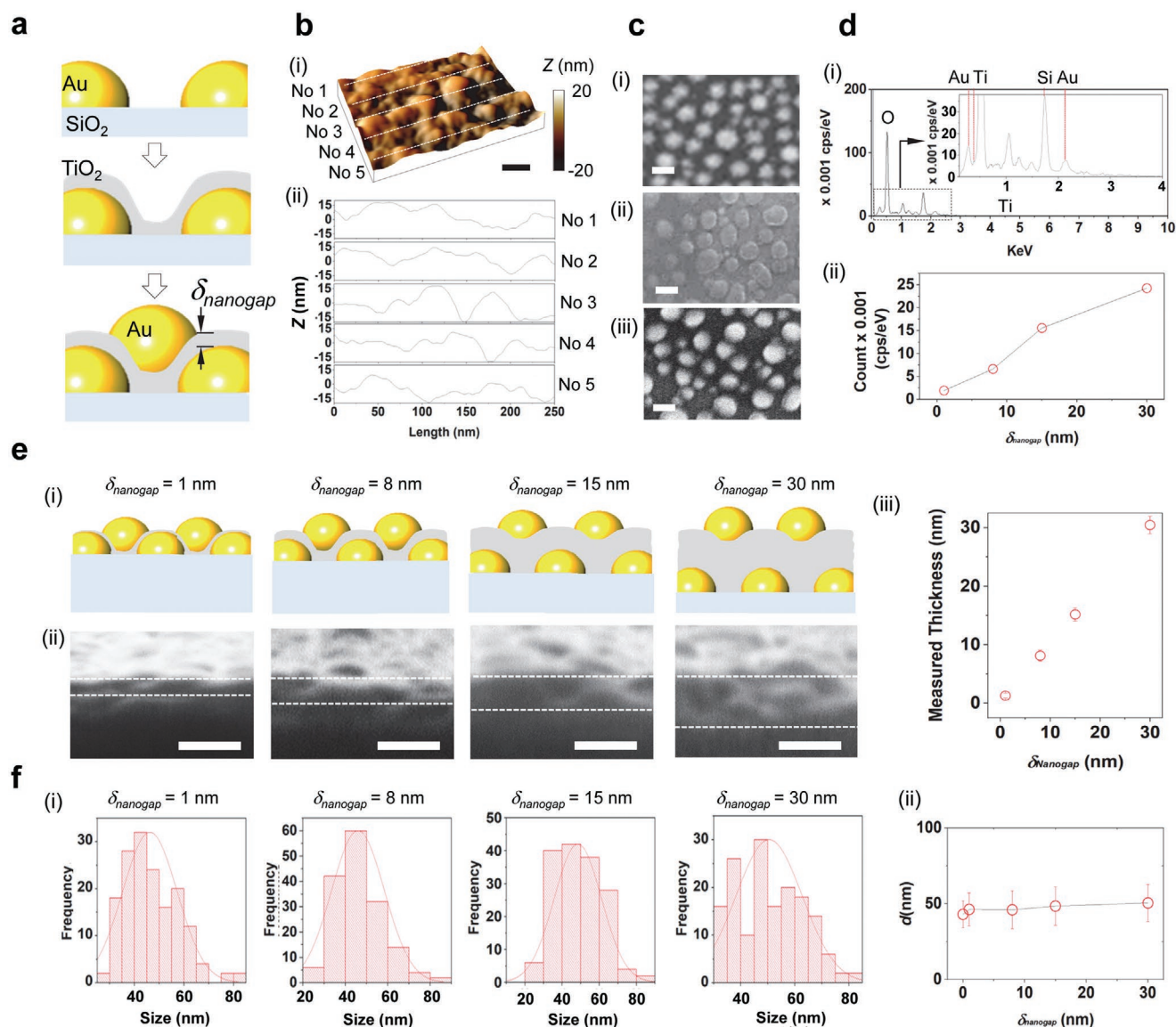### 2.2. Characterization of the Field Enhancement and Optical Properties

With the constructed PNA structures, we characterized the optical properties (**Figure 3**). First, we estimated the local
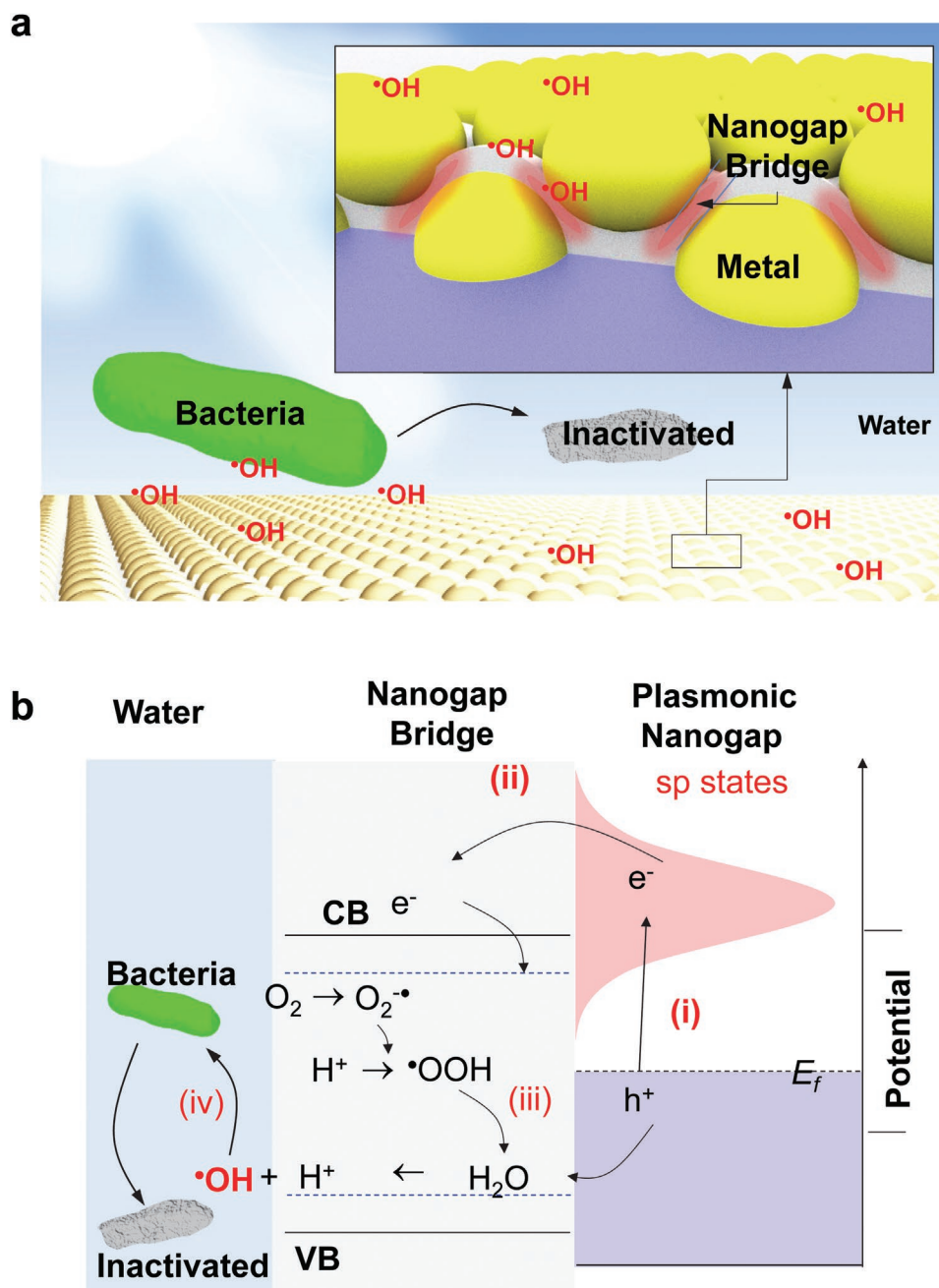
Figure 1. Visible light induced water treatment with PNA. a) Schematic that shows that plasmonic nanogap bridged by semiconductor nanolayer with interacting bacteria in water through visible-light photocatalytic ROS generation. The nanogap plays roles in visible light focusing and charge separation to maximize the ROS generation. b) Mechanism of nanogap assisted PRET with energy levels on charge separation. Blue lines indicate the energy level for surface ROS (ex. OH radicals) generation. This mechanism involves following steps; i) Nanogap assisted SP state which is excited from electrons around the Fermi level (E_f) of the metallic structure, ii) the transfer of the excited hot electrons to a neighboring TiO$_2$ nanostructure, iii) charge separation between valance band (VB) and conduction band (CB) induced ROS generation, and iv) Bacteria inactivation by the generated ROS.

electric (E)-field distribution and its enhancement (= $|E_n/E_0|^2$, where E_0 is the base E-field intensity and E_n is the enhanced electric field intensity) around the representative PNA structure using a finite element analysis (FEA) (see Supporting Information) (Figure 3a,b). Under visible-light illumination ($\lambda = 650$ nm), the PNA showed a strong E-field

focusing in the nanogap owing to the strong plasmonic coupling inducing a power transfer. On the other hand, the AuNS and TiO$_2$/AuNS revealed a focused E-field around the edge of the AuNS. With the FEA results, we measured the optical properties of AuNS, TiO$_2$/AuNS, and PNA (Figure 3c). First, the AuNS array resulted in a resonance

ADVANCED
SCIENCE NEWS
www.advancedsciencenews.com

NANO · MICRO
small
www.small-journal.com

Figure 2. Characterization of multidimensional plasmonic nanogap bridged with a semiconductor layer in a large area substrate. a) Schematic shows the fabrication procedure of PNA. b) i) AFM image and ii) profiles of PNA ($\delta_{nanogap}$ = 8 nm) (scale bar = 50 nm) c) SEM images of i) AuNS array, ii) TiO2/AuNS, and (ii) PNA ($\delta_{nanogap}$ = 8 nm) (scale bar = 50 nm), and (iii) cross-section of the PNA as a function of $\delta_{nanogap}$ from 1 to 30 nm (scale bar = 50 nm). d) i) EDS spectrum of PNA ($\delta_{nanogap}$ = 8 nm) and ii) Ti counts as a function of $\delta_{nanogap}$ from 1 to 30 nm. e) i) Cross-sectional schematics, ii) SEM images, and iii) TiO2 thickness of PNAs on glass substrates as a function of $\delta_{nanogap}$ from 1 to 30 nm. f) Quantification of the morphology of PNAs: i) average sizes and ii) average diameter of AuNS as a function of $\delta_{nanogap}$ from 1 to 30 nm.

peak at 580 nm. Then, layering the TiO$_2$ nanolayer (δ_{TiO_2} = 8 nm) on the AuNS array led a redshift owing to the higher reflective index of TiO$_2$. The nanogap of TiO$_2$ layer does not reveal any optical extinction in the visible range. The optical properties of the PNA structure indicate that the nanogap of TiO$_2$ layer induces nano plasmonic coupling and highly enhanced visible-light absorption. To explore the effect of the plasmonic nanogap of TiO$_2$ nanolayer on a channel for plasmon-pathway, we further characterized the optical properties of the PNA structure as a function of the $\delta_{nanogap}$ from 1 to 30 nm (Figure 3d). The LSPR peak shifted from 750 to 530 nm with the $\delta_{nanogap}$. The highest extinction occurred around $\delta_{nanogap}$, 8 nm. Furthermore, we compared

maximum intensity of the scattering and extinction spectra as a function of $\delta_{nanogap}$ (Figure 3e). We used a dark-field microscope to acquire scattering spectra (see Experimental Section). The scattering intensity (I_{scat}) decreased with $\delta_{nanogap}$ as we observed in the FEA results. Meanwhile, the highest extinction intensity (I_{ext}) is shown around $\delta_{nanogap}$ = 8 nm which is comparable to the charge diffusion distance in the TiO$_2$ structure.[14,23] The plasmonic nanogap of TiO$_2$ functions as a channel that induces plasmon decay, forming energetic charge carriers (e–h pairs). The TiO$_2$ nanolayer between the coupled AuNS arrays leads to the generation of hole-electron pairs and it becomes a critical plasmon-pathway.

**ADVANCED
SCIENCE NEWS**
www.advancedsciencenews.com

NANO · MICRO
small
www.small-journal.com
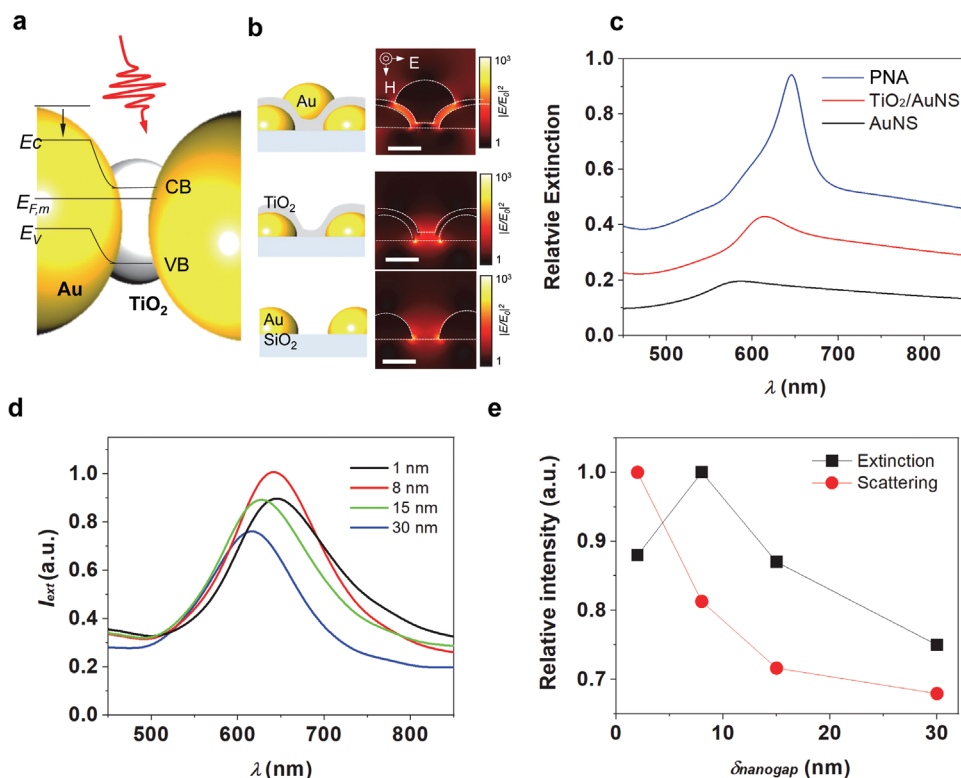
Figure 3. Optical properties of the multidimensional PNA. a) Schematic of visible light focusing and charge separation in the PNA. The nanogap between AuNS layer of the PNA leads to plasmonic coupling. The nanogap is filled with a TiO_2 nanolayer. b) Distribution of E- field around the AuNS array, TiO_2/AuNS array, and PNA at $\lambda = 650$ nm (Scale bar = 40 nm). c) Extinction spectra of AuNS, TiO_2/AuNS, and PNA. d) Measured extinction spectrum as a function of $\delta_{nanogap}$ from 1 to 30 nm. e) Comparison between absorption and scattering spectra as a function of $\delta_{nanogap}$ from 1 to 30 nm.

2.3. Hydroxyl Radical Generation

The strong visible-light absorbance of the PNA is expected to result in a rapid charge transfer to the TiO_2.[7,8,10,20,21] Charge separation in the TiO_2 layer leads to surface reactions that generate $\cdot$OH at the interface of the AuNS, TiO_2, and H_2O (**Figure 4**). In plasmonic-semiconductor nanostructures, when LSPR exists in the AuNS under light illumination, through hot electronic injection, energetic and ballistic electrons generated inside the AuNS are injected into the conduction band of the TiO_2 layer. In this interfacial electron transition, electrons in the metal are directly excited to a level in the semiconductor, typically from the Fermi level of the AuNS to the conduction band of the TiO_2. The pair of electric charges thus separate, namely a negative one in the TiO_2 conduction band and a positive one in the AuNS, and have electrochemical energy, which can be further converted into chemical energy (e.g., hydroxyl radicals, $\cdot$OH) for water treatment (Figure 4a).

To confirm $\cdot$OH generation under visible light illumination (Figure S3, Supporting Information), we performed a photocatalytic $\cdot$OH generation test and we adopted a chemical transformation reaction of terephthalic acid (TA) to 2-hydroxyterephthalic acid (TAOH) (Figure 4b). This reaction was used to estimate $\cdot$OH generation. The reaction between single OH radicals and TA molecules produced single fluorescence TAOH molecules (excitation wavelength (λ_{ext}) = 450 nm and emitting wavelength (λ_{emit}) = 475 nm) (see Experimental Section).[24] In this test, the

PNA was integrated into a polydimethylsiloxane (PDMS) microfluidic chamber (see Experimental Section). Under visible-light illumination[18,25,26] (light intensities, I = 200 mW cm^{-2}) at TA concentration (C_{TA}) = 100 μM, we compared OH radical generation from PNA (R_{OH_ATA}) with that from AuNS and TiO_2/AuNS, individually. The R_{OH_ATA} (= 5.6×10^{-10} M min^{-1}) shows faster OH radical generation than that R_{OH_A} (= 2.2×10^{-1} M min^{-1}) and R_{OH_TA} (= 0.7×10^{-1} M min^{-1}). The combined effect of the plasmonic coupling and the charge separation in the plasmonic nanogap of TiO_2 layer led to the enhanced OH radical generation performance. Under dark condition, we did not observe any noticeable OH radical generation from any of the samples.

2.4. Visible Light-Induced Photocatalytic Performance

For the quantification of OH radical, a high pH solution (pH ≈ 13) was used to dissolve the TA due to low solubility (0.0015 g/100 mL at 20 °C). This high pH condition is also desirable to enhance conversion of the photocatalytic reaction on TiO_2 surface,[27,28] however, the pH condition limits the practical water treatment model to pH = 5–9.[29] In this consideration, we continued tests of a methylene blue (MB) decomposition (see Method section). First, we confirmed visible light effect on the conversion of MB degradation (Figure 4c). In this test, we integrated the PNA into a polydimethylsiloxane (PDMS) microfluidic chamber (Figure S4, Supporting Information). The

ADVANCED
SCIENCE NEWS
www.advancedsciencenews.com

NANO · MICRO
small
www.small-journal.com
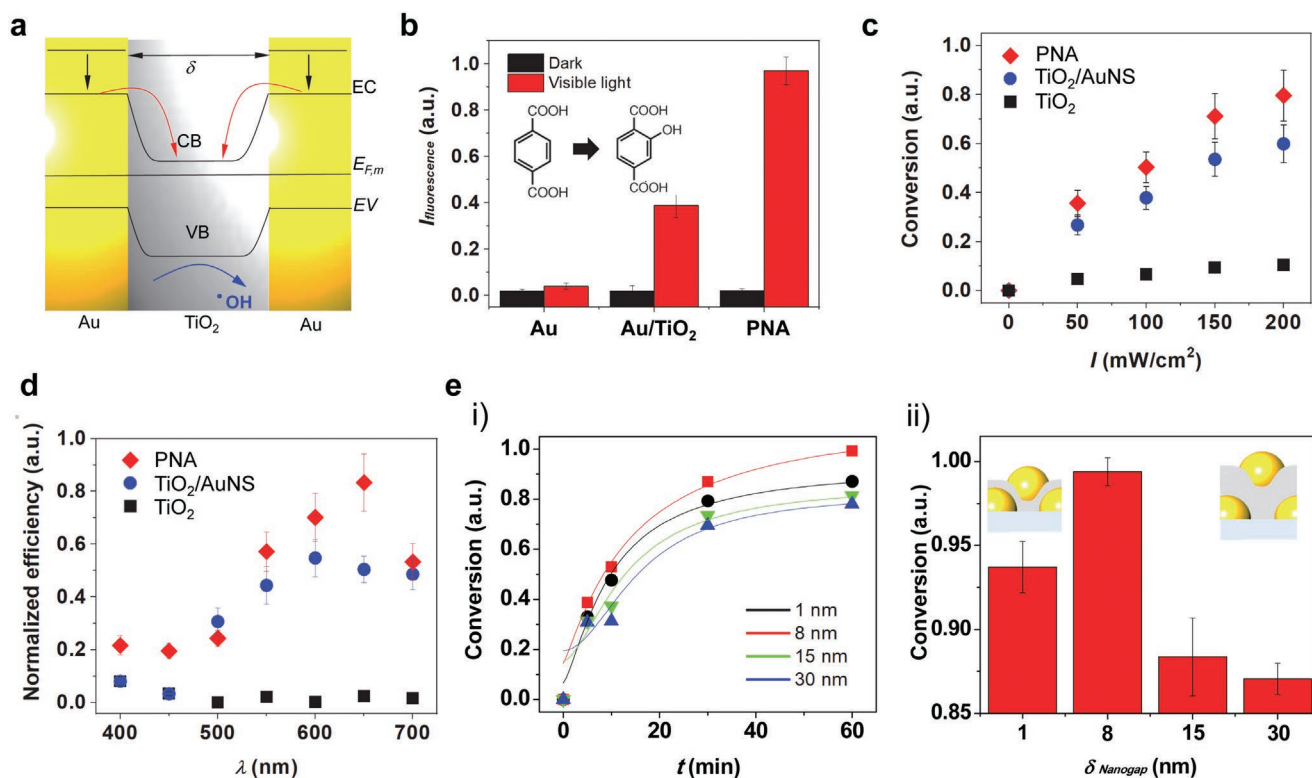
Figure 4. Visible light-induced photocatalytic performance in PNA. a) A schematic diagram of charge separation and radical generation though the plasmonic nanogap of TiO_2 between AuNSs. b) Quantification of OH radical generation; fluorescent intensity of the sample solutions prepared at pH 12.5 containing TA and 0.1 M Na_2SO_4 at $I = 200$ mW cm^{-2} for 2 h. c) Conversion of photocatalytic MB decomposition under visible illumination in the AuNS, TiO_2/AuNS, and PNA ($\delta_{nanogap} = 8$ nm) nanostructures as a function of light intensity (I) from 0 (dark) to 200 mW cm^{-2} at $Q = 2.0$ mL min^{-1}. d) Normalized efficiency of photocatalytic MB decomposition as a function of filter cut-off wavelength in the TiO_2, TiO_2/AuNS, and PNA ($\delta_{nanogap} = 8$ nm) nanostructures at TiO_2, TiO_2/AuNS, and PNA at $Q = 2.0$ mL min^{-1} and $I = 200$ mW cm^{-2}. The normalized efficiency was estimated by normalization of the ratio between MB decomposition rate and number of photon absorption rate at each filter cut-off wavelength. Error bars represent the standard deviation of the systematic errors in the collection of spectrum data. e) Nanogap effect on MB decomposition. i) Dynamics of photocatalytic performance as a function of $\delta_{nanogap}$ from 1 to 30 nm at $Q = 2.0$ mL min^{-1} and $I = 200$ mW cm^{-2}. ii) Conversion of MB decomposition as a function of $\delta_{nanogap}$ from 1 to 30 nm at $Q = 2.0$ mL min^{-1} and $I = 200$ mW cm^{-2}.

conversion of MB degradation, *Conv* (= $(C_{MB0}-C_{MB})/C_{MB0}$, where C_{MB0} and C_{MB} are the MB concentrations before and after the reaction, respectively) revealed sensitive increases with the I_{light} from 50 to 200 mW cm^{-2} in PNA compared to those in TiO_2/AuNS and TiO_2, which showed less sensitivity at the same condition. In particular, PNA structure with $\delta_{nanogap} = 8$ nm led to *Conv* of 99%, meanwhile 56% and 30% were obtained in TiO_2/AuNS and TiO_2, respectively, at $I = 200$ mW cm^{-2}. Furthermore, to confirm the visible light-induced photocatalytic activity of the PNA, we plotted the *Conv* as a function of incident wavelengths between 400 and 700 nm (Figure 4d). Specifically, at $\lambda = 650$ nm, we observed the maximum *Conv* (≈90%) in PNA, while TiO_2/AuNS and TiO_2 resulted in *Conv* of ≈70 and ≈20% at $\lambda = 600$ and 400 nm, respectively. This spectrum dependence of MB degradation is consistent with the characterized absorption spectrum in Figure 3.

When the plasmonic coupling solely contributed the photocatalytic reaction, narrower nanogap will result in higher rate of ·OH generation. However, since charge separation occurs in the TiO_2 nanogap, simultaneously, a dimension of TiO_2 nanogap enabling efficient diffusion of the separated charges must be considered to maximize ·OH. The separated charge carrier transfer is involved in the charge-carrier diffusion length. In this consideration, we estimated the TiO_2 nanolayer effect on the MB decomposition by varying the $\delta_{nanogap}$ from 1 to 30 nm (Figure 4e). The highest *Conv* of ≈98% at $\delta_{nanogap} = 8$ nm occurred after 60 min reaction. When $\delta_{nanogap}$ increased to 30 nm, ξ gradually decreased to ≈51%. However, when $\delta_{nanogap}$ was thin (= 1 nm), we observed *Conv* = 75%, which was lower than that with $\delta_{nanogap} = 8$ nm. In the below 10 nm range, a discrepancy between the plasmonic nanogap of TiO_2 layer and the minority charge diffusion length occurred.[23] Plasmonic coupling was stronger in the thin TiO_2 layer, but the charge diffusion cannot be maximized due to the low charge separation. On the other hand, in the case of thick $\delta_{nanogap}$ (>8 nm), although a wider plasmonic nanogap of TiO_2 layer induced larger charge diffusion, the plasmonic coupling was lowered. Accordingly, to maximize the combined effects of the plasmonic nanogap and the charge diffusion in the TiO_2 nanolayer between two AuNS arrays, we optimized the TiO_2 layer thickness ($\delta_{nanogap} = 8$ nm) for simultaneous light harvesting and OH radical generation under visible light. The E-field in the PNA at $\delta_{nanogap} \approx 8$ nm resulted in a rapid charge separation comparing the AuNS and TiO_2/AuNS (Figure S5, Supporting Information) as well as a faster photocatalytic reaction rate.

2.5. Visible Induced Bacteria Inactivation

We turned to visible light induced inactivation of bacterial particles in water based on the mechanism of photocatalytic performance enhanced by PNA (**Figure 5**). The visible induced •OH generation from PNA expected to damage the membrane of bacterial particles in water (Figure 5a). The tests were performed in the PNA integrated microfluidic reactor to enable straightforward setup and operation for a potential solar panel design (see Experimental Section). In this test, as a representative water pathogen model, we used *Escherichia coli* (*E. coli*) K-12 ($\approx 5 \times 10^6$ CFU) in a tap water-based medium (Washtenaw County, MI USA) (see Experimental Section). First, to confirm the photocatalytic inactivation, we characterized the *E. coli* morphology by obtaining SEM images (Figure 5b). The PNA ($\delta_{nanogap} = 8$ nm) under the *E. coli* sample was treated under light illumination ($I = 200$ mW cm^{-2}) for 90 min. We observed membrane damage in which pores were formed by OH radicals. This inactivation of treated *E. coli* by the PNA was quantified by estimating $-\log N/\log N_0$ (N and N_0 are the *E. coli* populations before and after the treatment, respectively), and we compared between the control, AuNS array, and TiO$_2$/AuNS array (Figure 5c). PNA was the most effective for inactivating *E. coli*. PNA was the most broadly effective material, able to achieve a 6-log inactivation of *E. coli*, and a 4.7 and 4.1- log inactivation in 60 min illumination. The $-\log N/\log N_0$ value of

AuNS array indicates that photothermal effect is involved in the inactivation of *E. coli*.

In the PNA structure, if the photothermal effect on the *E. coli* inactivation is significant, narrower nanogap leading to larger photothermal effect owing to focused *E*-field will result in higher performance in *E. coli* inactivation. On the other hand, if the photocatalytic effect is dominant, the inactivation performance will follow the trends of OH radical generation as a function of $\delta_{nanogap}$. To confirm this, we tested the effect of nanogap thickness and I on the inactivation performance by estimating $-\log N/\log N_0$ by varying the $\delta_{nanogap}$ from 1 to 30 nm (Figure 5d). The lowest log $N/\log N_0$ of -5 at $\delta_{nanogap} = 8$ nm under the same light illumination condition was observed. This *E. coli* deactivation trends is similar to that of MB decomposition. This result clearly indicates that the combined mechanism of larger light absorption and charge transfer led to such high inactivation.

Considering the optofluidic performance, to investigate retention time effect, we further evaluated the *E. coli* inactivation performance as a function of flow rate (Q) ranging from 1 to 20 mL min^{-1} (Figure 5e). In this optofluidic panel test, this range of flow rates was determined according to the average volume of graywater production per day in a single family household in the USA.[30,31] In general, μ_D decrease with Q, and the highest μ_D was observed at $\delta_{nanogap} = 8$ nm and $Q = 1$ mL min^{-1}. Taken together, these results successfully
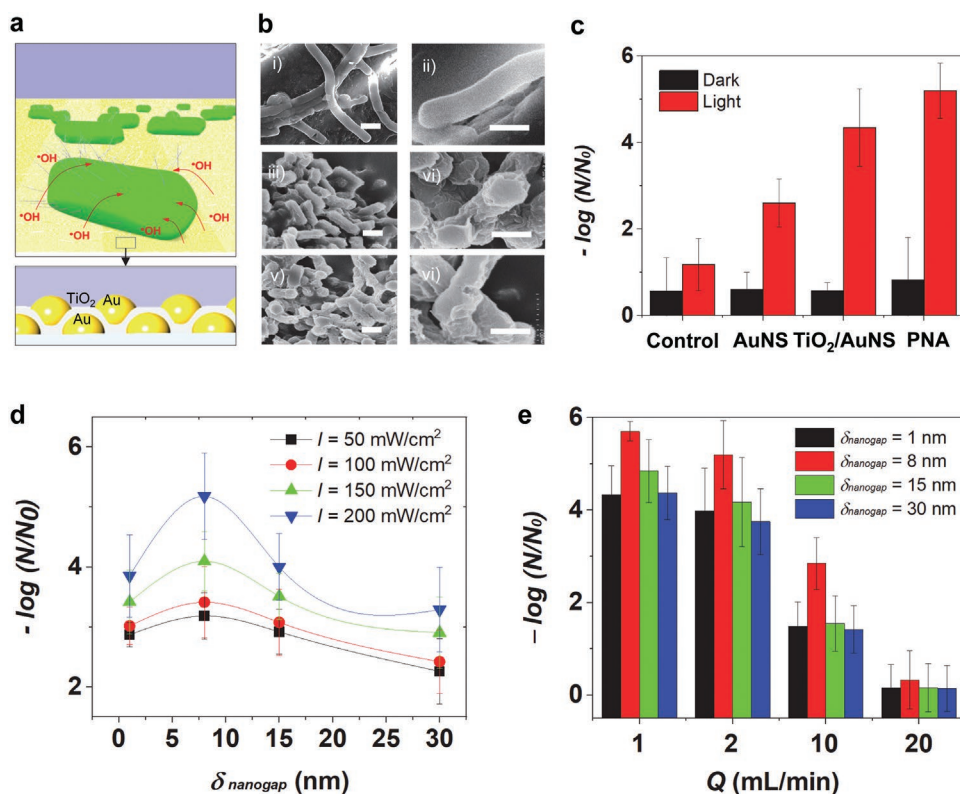
Figure 5. Visible light-induced water inactivation. a) Schematic of interaction between the generated OH radicals from PNA and *E. coli* under visible light illumination. b) SEM images of *E. coli* without any treatment (i,ii), treated with AuNSs (iii,iv), and treated with PNA (v,vi) (scale = 0.5 µm). c) *E. coli* inactivation on control, AuNS, TiO$_2$/AuNS, and PNA with $\delta_{nanogap} = 8$ nm at dark and light on ($I = 200$ mW cm^{-2}) after 60 min. d) *E. coli* inactivation as a function of $\delta_{nanogap}$ from 1 to 30 nm with varying I from 50 to 200 mW cm^{-2} at $Q = 2.0$ mL min^{-1} under visible-light illumination. e) *E. coli* inactivation performance as a function of Q from 1 to 20 mL min^{-1} at $I = 200$ mW cm^{-2} with $\delta_{nanogap}$ varying from 1 to 30 nm.

demonstrate visible-light-induced 5-log N/N_0 water disinfection and 100% chemical decomposition for the sustainable water treatment.

3. Conclusions

In this study, we studied highly sustainable solar water inactivation with the multidimensional PNA structure. The multidimensional PNA allowed significantly enhanced visible-light focusing and rapid charge separation for rapid OH radical generation. In this multidimensional geometric arrangement, the TiO_2 nanolayer between the two layers of the AuNS array played the critical roles of i) a plasmonic nanogap enhancing local electric field, ii) a diffusion channel for separated charge carriers, and iii) active sites for catalytic generation of OH radicals. Through the geometric arrangement of the TiO_2 nanolayer in the plasmonic coupling, we successfully demonstrated that optimizing the charge carrier length in the plasmonic nanogap of the TiO_2 layer led to highly enhanced *E. coli* inactivation. The PNA potentially targets an optofluidic panel for solar water treatment by introducing scale-up method. Similar to a conventional solar panel, which converts sunlight into electrical energy, the thin optofluidic panel with PNA integration can be potentially installed on the exteriors of houses or buildings. The PNA will be integrated into the optofluidic platform, and, under sunlight illumination, the flow of the contaminated water on the metal semiconductor structure enables recycling of the treated water. We expect that the integrated optofluidic panel will be widely used to treat low-contaminated water (e.g., graywater) from buildings and houses owing to its energy sustainability, set-up flexibility, and scalability (Figure S6, Supporting Information).

4. Experimental Section

Materials: TAOH, TA, MB, sodium hydroxide (NaOH) were purchased from Sigma Aldrich Inc. PDMS were purchased from Dow chemicals Inc. The high-purity water used was distilled, deionized and then purified with the Milli-Q system (Nippon Millipore Co., Tokyo).

PNA Fabrication: After Au deposition on a clean SiO_2 substrate (four-inch wafer), a dewetting step was performed at 450 °C for 10 min using lamp-heated rapid thermal process (RTP) (Jetfirst RTP 150) (see Supporting Information). After confirming the uniform AuNS array, TiO_2 nanolayer was layered using E-beam evaporation (Angstrom Engineering Evovac Evaporator) on top of the AuNS. To ensure crystallinity of the TiO_2 layer,[22,32] the sample was annealed at 400 °C for 1 h. Another AuNS layer was then constructed on top of the TiO_2/AuNS at the same condition as for the first the AuNS layer.

Characterization of Morphologies and Optical Properties: Morphologies of the PNA samples were analyzed by SEM images, Image J, and AFM (see Supporting Information). The optical properties of PNA was characterized by a dark-field microscope with a dark field condenser lens (NA = 1.45, MBL12000, Nikon). Global optical properties of the samples were measured by a UV–vis spectrometer (Agilent 8453).

Construction of the Integrated Optofluidic Device: An optofluidic reactor consisting of an optical window and 5 × 5 micro pillar arrays in the reaction chamber area were designed (see Supporting Information). The optofluidic reactor was fabricated according to the PDMS based soft-lithography process.

Quantification of Hydroxyl Radicals: A stand scavenger reaction was employed (see Supporting Information). Chemical transformation of TA with the generated OH radicals resulted in the formation of TAOH (see Supporting Information). By analyzing the TAOH which are fluorescent molecules in the treated sample, the generated OH radical quantified. The TAOH analyses were performed using a microplate reader (BioTek, Inc.).

Visible Light Induced Photocatalytic Reaction: The photocatalytic activity of the system in the optofluidic reactor was estimated under visible light illumination (Dolan-Jenner Fiber-Lite 180 with a 150 W, 21 V halogen (EKE) lamp) (see Supporting Information). The flow rate of the solution into an optofluidic reactor was controlled by using a syringe pump (Cole Palmer, EW-74900-00). The treated sample solution was analyzed using a UV-vis absorbance spectrometer (Agilent Technologies, Inc.) and microplate reader.

E. coli Inactivation Test: The cultured bacteria were added to 10 mL of Luria-Bertani (LB) broth and incubated (see Supporting Information). Using an OD meter, a portion of the solution containing the bacteria was diluted to ≈5 × 10^6 CFU/mL with tap water. Under visible light illumination, the prepared *E. coli* sample was flowed in the reactor. The treated *E. coli* solution was collected through the outlet of the optofluidic reactor into a microtube. *E. coli* samples were characterized and quantified: i) after the dehydration of the treated *E. coli*, SEM images were obtained, and ii) the number of inactivated *E. coli* were quantified using a standard spread-plate counting method.

Model Local Electric (E) Field Distribution: FEA (COMSOL Multiphysics software) was used (see Supporting Information) to characterize *E*-field around the PNS, AuNS, and TiO_2/AuNS. Based on the obtained SEM images, representative geometry of the PNA (Au diameter = 40 nm, Au thickness = 20 nm, and interparticle distance = 40 nm) was defined and thickness of TiO_2 layer was changed from 1 to 30 nm. *E*-field and energy around the PNA, AuNS, and TiO_2/AuNS was estimated as a function of wavelength and direction of the incident light.

Supporting Information

Supporting Information is available from the Wiley Online Library or from the author.

Conflict of Interest

The authors declare no conflict of interest.

**ADVANCED
SCIENCE NEWS**

www.advancedsciencenews.com

NANO · MICRO

small

www.small-journal.com

[1] C. Clavero, *Nat. Photonics* **2014**, *8*, 95.

[2] C. Hägglund, G. Zeltzer, R. Ruiz, I. Thomann, H.-B.-R. Lee, M. L. Brongersma, S. F. Bent, *Nano Lett.* **2013**, *13*, 3352.

[3] K. Kimura, S. Naya, Y. Jin-nouchi, H. Tada, *J. Phys. Chem. C* **2012**, *116*, 7111.

[4] M. Murdoch, G. I. N. Waterhouse, M. A. Nadeem, J. B. Metson, M. A. Keane, R. F. Howe, J. Llorca, H. Idriss, *Nat. Chem.* **2011**, *3*, 489.

[5] J. B. Priebe, M. Karnahl, H. Junge, M. Beller, D. Hollmann, A. Brückner, *Angew. Chem., Int. Ed.* **2013**, *52*, 11420.

[6] Y.-C. Pu, G. Wang, K.-D. Chang, Y. Ling, Y.-K. Lin, B. C. Fitzmorris, C.-M. Liu, X. Lu, Y. Tong, J. Z. Zhang, *Nano Lett.* **2013**, *13*, 3817.

[7] P. Christopher, H. Xin, S. Linic, *Nat. Chem.* **2011**, *3*, 467.

[8] P. Christopher, H. Xin, A. Marimuthu, S. Linic, *Nat. Mater.* **2012**, *11*, 1044.

[9] W. R. Erwin, H. F. Zarick, E. M. Talbert, R. Bardhan, *Energy Environ. Sci.* **2016**, *9*, 1577.

[10] J. Li, S. K. Cushing, F. Meng, T. R. Senty, A. D. Bristow, N. Wu, *Nat. Photonics* **2015**, *9*, 601.

[11] S. Mukherjee, L. Zhou, A. M. Goodman, N. Large, C. Ayala-Orozco, Y. Zhang, P. Nordlander, N. J. Halas, *J. Am. Chem. Soc.* **2014**, *136*, 64.

[12] A. Manjavacas, J. G. Liu, V. Kulkarni, P. Nordlander, *ACS Nano* **2014**, *8*, 7630.

[13] K. Wu, J. Chen, J. R. McBride, T. Lian, *Science* **2015**, *349*, 632.

[14] R. G. Zika, W. J. Cooper, *Photochemistry of Environmental Aquatic Systems*, ACS, Washington, DC **1987**.

[15] B. C. Hodges, E. L. Cates, J.-H. Kim, *Nat. Nanotechnol.* **2018**, *13*, 642.

[16] S. Griffin, N. P. Montoni, G. Li, P. J. Straney, J. E. Millstone, D. J. Masiello, J. P. Camden, *J. Phys. Chem. Lett.* **2016**, *7*, 3825.

[17] A. M. Brown, R. Sundararaman, P. Narang, W. A. Goddard, H. A. Atwater, *ACS Nano* **2016**, *10*, 957.

[18] C. Boerigter, R. Campana, M. Morabito, S. Linic, *Nat. Commun.* **2016**, *7*, 10545.

[19] M. Bernardi, J. Mustafa, J. B. Neaton, S. G. Louie, *Nat. Commun.* **2015**, *6*, 7044.

[20] M. Bernardi, M. Palummo, J. C. Grossman, *Nano Lett.* **2013**, *13*, 3664.

[21] S. A. Maier, H. A. Atwater, *J. Appl. Phys.* **2005**, *98*, 011101.

[22] K. Nakata, A. Fujishima, *J. Photochem. Photobiol., C* **2012**, *13*, 169.

[23] S. Girish Kumar, L. Gomathi Devi, *J. Phys. Chem. A* **2011**, *115*, 13211.

[24] Y. Nakabayashi, Y. Nosaka, *Phys. Chem. Chem. Phys.* **2015**, *17*, 30570.

[25] C. Boerigter, U. Aslam, S. Linic, *ACS Nano* **2016**, *10*, 6108.

[26] S. Linic, U. Aslam, C. Boerigter, M. Morabito, *Nat. Mater.* **2015**, *14*, 567.

[27] Y. Nakabayashi, Y. Nosaka, *Phys. Chem. Chem. Phys.* **2015**, *17*, 30570.

[28] J. Schneider, M. Matsuoka, M. Takeuchi, J. Zhang, Y. Horiuchi, M. Anpo, D. W. Bahnemann, *Chem. Rev.* **2014**, *114*, 9919.

[29] M. Oteng-Peprah, M. A. Acheampong, N. K. deVries, *Water, Air, Soil Pollut.* **2018**, *229*, 255.

[30] M. P. Gutierrez, L. P. Lee, *Science* **2013**, *341*, 247.

[31] O. R. Al-Jayyousi, *Desalination* **2003**, *156*, 181.

[32] K. Tanaka, M. F. V. Capule, T. Hisanaga, *Chem. Phys. Lett.* **1991**, *187*, 73.

2006044 (9 of 9)